Journal of Tissue Viability 35 (2026) 101006

Contents lists available at ScienceDirect

Journal of Tissue Viability

journal homepage: www.elsevier.com/locate/jtv

A robotic wound care patient for evidence-based surgical site infection research

Yael Shlomo [a], Aleksei Orlov [a], Ida Kreychman [a], Amit Gefen [a,b,c,d,*]

[a] School of Biomedical Engineering, Faculty of Engineering, Tel Aviv University, Tel Aviv, Israel
[b] Skin Integrity Research Group (SKINT), University Centre for Nursing and Midwifery, Department of Public Health and Primary Care, Ghent University, Ghent, Belgium
[c] Department of Mathematics and Statistics and the Data Science Institute, Faculty of Sciences, Hasselt University, Hasselt, Belgium
[d] Susan Wakil School of Nursing and Midwifery, Faculty of Medicine and Health, University of Sydney, Sydney, Australia

ARTICLE INFO

Keywords:
Bioengineering laboratory methods
Infection modeling
Preclinical research
Postoperative dressing
Bacterial colonization

ABSTRACT

Background: Surgical site infections (SSIs) are among the most common and preventable postoperative complications, yet existing preclinical models lack physiological realism and do not enable quantitative assessment of bacterial behavior. Wound pH critically modulates bacterial morphology and organization, underscoring the need for systems that replicate controlled wound environments.
Objectives: To develop and validate a robotic wound care patient (RWCP) that reproduces SSI-relevant physical and biological conditions, and to quantify pH-dependent bacterial morphology and spatial organization on wound dressings using automated deep-learning image analysis.
Methods: A life-sized abdominal RWCP integrating layered soft-tissue simulants, respiration simulation, controlled exudate delivery, and a laparotomy incision was engineered. Simulated wound fluid inoculated with *Lactobacillus delbrueckii subsp. bulgaricus* was delivered at pH 5.8 (acidic) or pH 6.8 (mildly acidic). Dressing samples were imaged with SEM, and bacterial morphology and topology quantified using a Cellpose-based deep-learning model, FIJI macros, and Python algorithms. Outcome measures included bacterial count, area coverage, circularity, roundness, aspect ratio, chain number, and bacteria per chain.
Results: Acidic pH increased bacterial counts by ~45% and produced morphological elongation (circularity and roundness ↓; aspect ratio ↑). Topological analysis identified nearly fourfold more bacterial chains and larger assemblies under acidic conditions ($p \leq 0.02$), indicating enhanced cooperative aggregation.
Conclusions: The RWCP provides a physiologically relevant, reproducible platform for SSI research, enabling sensitive detection of pH-driven bacterial morphological and organizational adaptations. This integrated mechanical-biological system offers a robust preclinical tool for evaluating wound care technologies and informing evidence-based SSI prevention strategies.

1. Introduction

Surgical site infections (SSIs) remain one of the most common and costly postoperative complications worldwide. In the United States, more than 10 million inpatients undergo surgery each year, representing over 25% of all hospital admissions, and SSIs account for ~36% of all healthcare-associated infections [1,2]. SSIs occur at or near the surgical incision within 30-90 days of surgery and remain largely preventable [3–6]. Nevertheless, despite modern aseptic techniques, SSIs still occur in 2%-10% of surgical procedures [3,7]. Laparotomies (abdominal surgeries), including cesarean delivery (C-section), carry the highest SSI risk [1,3,8]. Recent evidence from abdominal surgery indicates that SSIs are associated with increased mortality risk, with pooled odds ratios of 1.62 (95% CI 0.74-2.50) for incisional SSIs and 2.75 (95% CI 2.56-3.54) for organ/space SSIs, compared with non-SSI patients [9]. In addition, SSIs prolong hospitalization, increase costs, and worsen patient outcomes [10,11]. The predominant pathogens causing SSIs are Gram-positive bacteria, commonly *Staphylococcus aureus* [12]. Resistant bacterial strains, e.g., methicillin-resistant *Staphylococcus aureus* (MRSA), carry an approximately 20% mortality rate among affected patients [13,14].

The pathogenesis of SSIs is multifactorial, involving microbial contamination, impaired wound healing, and host immune response. Although strategies such as systemic antibiotic prophylaxis, improved surgical techniques, and antimicrobial dressings exist, they have not

* Corresponding author. School of Biomedical Engineering, Faculty of Engineering, Tel Aviv University, Tel Aviv, 6997801, Israel.
E-mail address: gefen@tauex.tau.ac.il (A. Gefen).

https://doi.org/10.1016/j.jtv.2026.101006
Received 6 December 2025; Received in revised form 13 March 2026; Accepted 21 April 2026
Available online 22 April 2026

Abbreviations

MRSA	Methicillin-resistant *Staphylococcus aureus*
NPWT	Negative pressure wound therapy
RWCP	Robotic wound care patient
SEM	Scanning electron microscopy
RCT	Randomized clinical trial
SD	Standard deviation
SSIs	Surgical site infections
SWF	Simulated wound fluid

eliminated SSIs, especially in high-risk or complex cases [15]. In routine clinical practice, sampling and analyzing wound fluid, without requiring a tissue biopsy, is the preferred method for obtaining culture specimens from surgical sites with suspected infection [16]. Traditional SSI management relies on silver-ion (Ag+) wound dressings and negative pressure wound therapy (NPWT), yet their effectiveness remains uncertain due to limited and low-certainty clinical evidence, heterogeneity across studies, higher costs of the NPWT, and persistent challenges in conducting robust randomized clinical trials (RCTs) [3,17,18]. Moreover, RCTs can be complex, costly, and logistically demanding, compounding the challenge of generating robust evidence for non-pharmaceutical wound care technologies [5,19–21]. Consequently, the strength and certainty of evidence supporting mainstream SSI prevention strategies remain limited. This underscores the need for standardized, reproducible preclinical models capable of evaluating wound care technologies under clinically relevant conditions [22,23]. Existing biological models, such as *ex vivo* porcine skin models [24,25] and *in vitro* biofilm assays [26,27], offer only partial insights and suffer from limited clinical relevance, high variability, and substantial cost [22,23,28].

Preclinical SSI models must account for key biological variables, particularly wound pH, which directly influences bacterial colonization, morphology and survival [29,30]. Acidic conditions drive adaptive bacterial morphologies such as filamentation and aggregation, and may support bacterial survival and biofilm formation [31–34]. *Lactobacillus delbrueckii subsp. bulgaricus*, widely used in dairy fermentation, is known to exhibit pH-dependent physiological responses [35–38]. This well-studied strain shifts from rounder to elongated morphologies and forms longer chains under acidic pH compared with neutral or alkaline conditions [39,40]. Critical pH thresholds were identified: moderate acidity slows division while maintaining culturability, whereas pH $\leq$ 3.5 induces marked elongation with incomplete septation [40,41]. Wound pH broadly influences the behavior of major wound pathogens; clinically, chronic wounds tend to remain alkaline, favoring biofilm growth and reducing antimicrobial efficacy, whereas acute wounds begin acidic and may shift toward neutrality if healing is impaired [29,30,42,43]. These findings indicate that wound pH is critically important in SSI prevention and management and support the use of *Lactobacillus delbrueckii subsp. bulgaricus* as an appropriate surrogate for evaluating the sensitivity of preclinical SSI models.

Another important aspect of a preclinical SSI model is the ability to track bacterial changes using computerized image processing, including automated cell segmentation, morphological analysis, chain detection, and counting [44]. Software developed for these purposes include BiofilmQ for high-throughput community-level image cytometry [45]; and deep-learning pipelines such as Mask R-CNN, DeepLabv3+, and Yolact for extracting geometric features from scanning electron microscopy (SEM) biofilm images [46,47]. Semi-automated quantitative approaches have also been described, including ImageJ/ObjectJ which resolves membrane- or DNA-stained chains into single cells and enable per-chain cell counts [48]. In *Streptococcus pneumoniae*, for example, chain length has been quantified microscopically, or with ImageJ, and linked to adherence, colonization, and competence induction [49,50]. For lactic acid bacterial strains, deep-learning-based image analysis of SEM micrographs quantified morphological adaptations of *Lactiplantibacillus plantarum* under acidic stress [39,40]. Clinical applications were further attempted, with Cellpose 3 for segmenting bacteria in Gram-stained blood smears from septic patients [51]. However, wound-dressing materials contaminated with bacteria were not yet investigated using advanced image processing approaches. Topological network analyses of bacterial interactions on dressings, documented in SEM images, would provide important insights and should be part of a preclinical model of SSI.

The published work of Gefen and his research team demonstrated the utility of robotic wound systems for efficacy research of various advanced dressings and single-use NPWT in fluid handling, enabling prediction of clinical performance of products in exudate management [52–56]. Their robotic wound models, developed for sacral and heel pressure injuries, diabetic foot ulcers, and venous leg ulcers, simulated anatomical shape, loading, soft-tissue mechanics, wound and skin temperatures, and continuous or bolus exudate flow using clinically realistic fluid properties. [52–54,56]. Primary and secondary dressings or single-use NPWT systems were applied and tested for hours to several days while simulant wound fluid (SWF) was delivered under controlled steady or pulsed flow. Temperature, flow and pressure sensors enabled real-time performance monitoring, and fluid uptake, mechanical integrity, and dressing durability were assessed post-use.

In this work, we extend this robotic wound concept for the first time to a hybrid, integrated mechanical-biological system for SSI research, referred to here as the *robotic wound care patient* (RWCP). The article describes the engineering design and validation of this RWCP with a laparotomy incision, incorporating a pH-controlled SWF inoculated with *L. delbrueckii subsp. bulgaricus* and enabling automatic SEM-based quantification of bacterial morphology and colonization behavior on wound dressings, using image processing tools and deep learning codes. This innovative RWCP represents a major advancement in SSI research: It can strengthen the preclinical evidence base, facilitate quantitative efficacy research of wound care technologies, support industry research and development, focus RCT designs, and ultimately, contribute to improved SSI prevention strategies.

2. Methods

2.1. Design and construction of the robotic wound care patient

The RWCP is a modular experimental phantom constructed to replicate SSI conditions under controlled physical and environmental conditions. The system is based on a life-sized 3D male torso (22 cm in length, 35 cm in width, and 53 cm in height) that integrates layered soft-tissue simulants, an incision site, bilateral lung cavities for simulated respiration, and embedded irrigation tubing for controlled wound fluid delivery. Wound exudation simulations are controlled through a multi-channel syringe pump system (Fig. 1a), while respiration is reproduced using internal balloon reservoirs inflated by air pumps (Fig. 1b). The system is controlled electronically and the wound conditions are monitored via integrated sensors as detailed below, allowing reproducible laboratory simulations of the clinical conditions associated with surgical wound care.

The RWCP was constructed using synthetic soft tissue simulants molded in a custom-designed gypsum-silicone casting assembly. The outer shell was constructed from solid gypsum, to provide structural support and stability during and after molding. The inner mold, which was specifically designed to accommodate embedded anatomical structures such as the simulated lungs and the incision module, was cast in silicone to ensure flexibility and anatomical fidelity in the soft tissue regions (Dragon Skin FX, Smooth-On, Macungie, PA, USA). The phantom creation included a removable 3D-printed incision structure (15 cm in length and 3 cm in depth) with irrigation channels, and lung cavity containers (Fig. 2a). The irrigation channels remain embedded in the

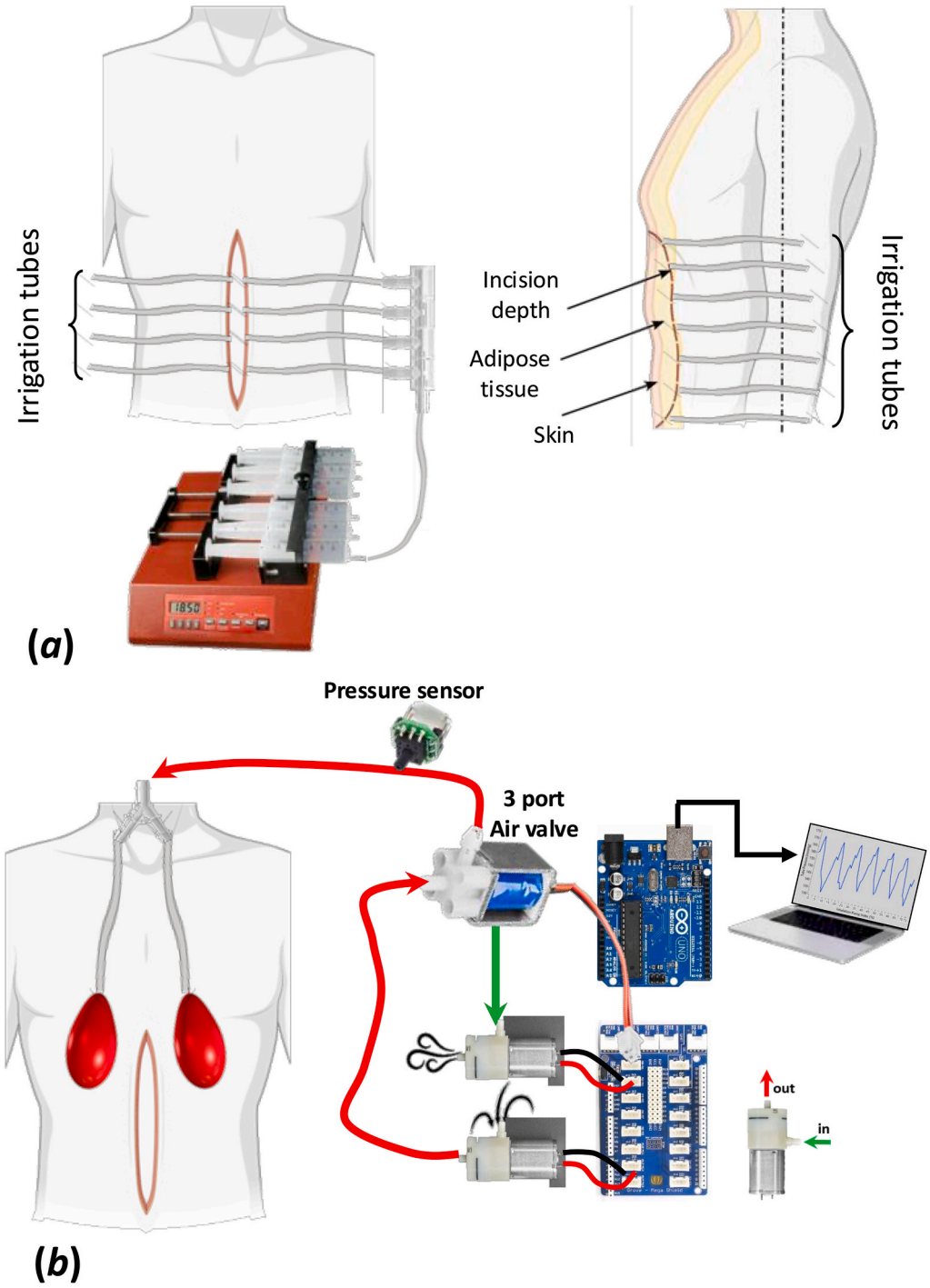

Fig. 1. Schematic diagram of the robotic wound care patient (RWCP) system design: (a) Frontal (left frame) and lateral (right frame) views, indicating the location of the surgical incision and configuration of the embedded, perforated irrigation tubing, which is connected to a multi-channel electromechanical syringe pump system for controlled simulated wound fluid delivery. (b) The mechanism facilitating simulation of respiratory movements in the RWCP, including the simulated lungs, inflated by means of a pump with its microcontroller system.

unit, whereas the incision structure and cavity containers are removable (Fig. 2b). The phantom consisted of three stratified layers mimicking abdominal soft tissue, fabricated using Dragon Skin FX silicone: a 2 mm-thick skin simulant layer, a 16 mm-thick adipose simulant layer incorporating a Slacker (Smooth-On, Macungie, PA, USA) additive to reduce hardness and mimic subdermal adipose tissue, and a base skeletal muscle simulant layer. According to the technical datasheets, and following the relevant testing standard ASTM D412-0616, the tensile strength and tangent modulus (at 100% strain) of the Dragon Skin 20 silicone material are approximately 3.8 MPa and 340 kPa, respectively. These silicone properties fall within reported ranges for macroscopic large-strain behavior of skin and muscle tissues [57–63]. The adipose simulant layer formulation with Slacker reduces these mechanical properties by an order of magnitude to mimic the softer nature of adipose tissue, which agrees with our reported stiffness measurements of native, freshly harvested adipose tissue [64] and is also in line with our previously published wound care robot designs [54].

After curing of the soft-tissue simulant materials, the balloon

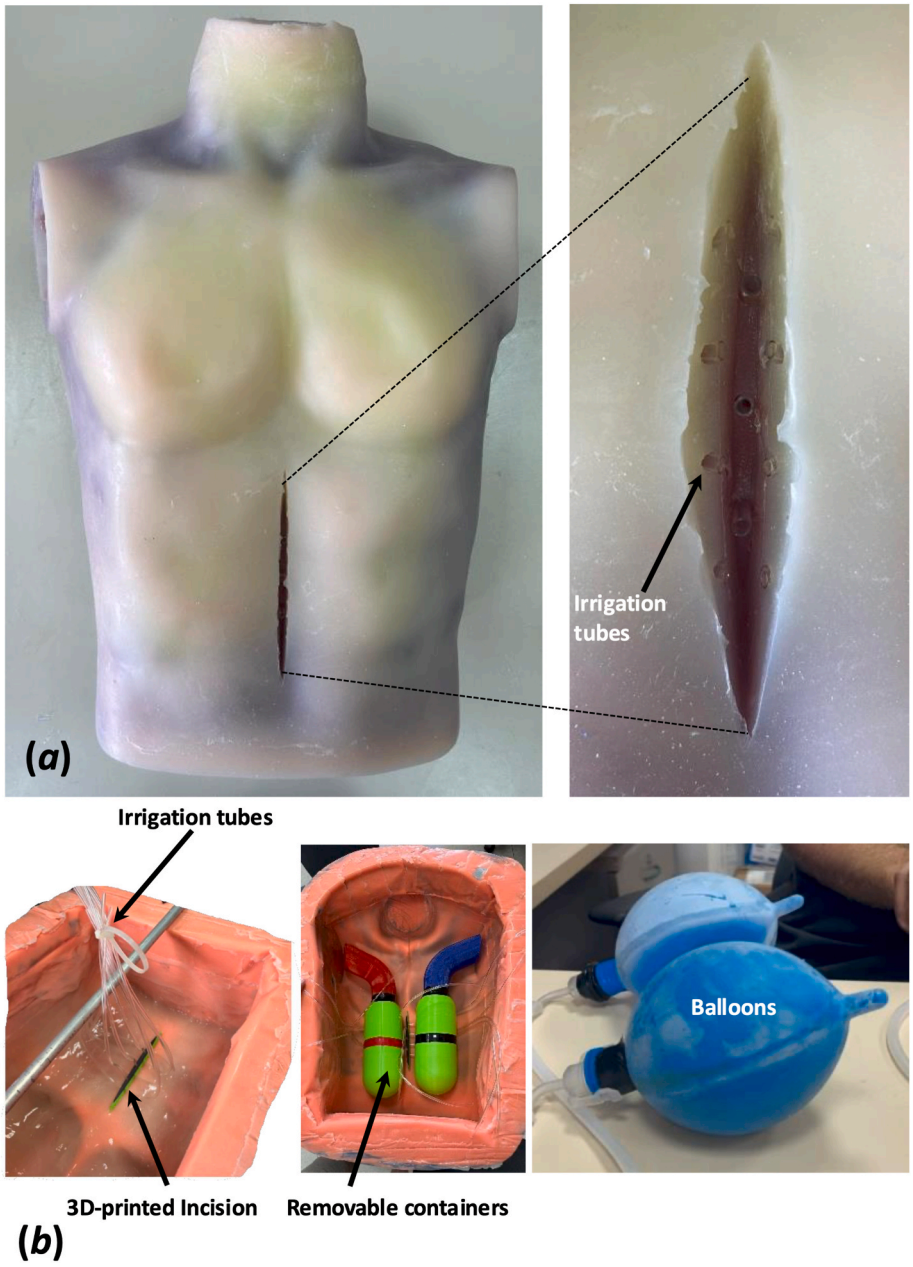

Fig. 2. The robotic wound care patient (RWCP) laboratory apparatus: (a) The RWCP includes a three-layer soft tissue simulant, with skin, adipose and skeletal muscle being represented, and an incision wound, embedded with irrigation tubing for release of simulated wound fluid. (b) The casting mold and modular components used for RWCP fabrication, including the removable 3D-printed incision structure and the lung cavity containers. The irrigation channels remain embedded in the unit, whereas the balloon reservoirs and cavity containers used for simulating the breathing movements are insertable and removable.

reservoirs and incision module were integrated to represent breathing dynamics and wound morphology, respectively. The system was further connected with the embedded irrigation tubing to a multi-channel electromechanical syringe pump (NE-1600, New Era Pump Systems Inc., Farmingdale, NY, USA) for accurate flow rate control of fluid delivery.

To simulate physiological respiration, including chest movements and intra-abdominal pressure variations, two 12 V DC air pumps (D2028 pump, SparkFun Electronics, Niwot, CO, USA) were used to inflate the internal balloons rhythmically, at a resting respiratory rate of 12-16 breaths/min. The entire system was controlled by an Arduino UNO R3 (Arduino AG, Somerville, MA, USA) microcontroller with feedback from a digital pressure sensor (XGZP6847A, CFSensor, Wuhu, China), monitored via LabVIEW software (2023Q3, National Instruments, Austin, TX, USA; URL: https://www.ni.com/labview) (Fig. 1b).

2.2. The simulated wound fluid and surgical site infection

The bacterial model used in this study was based on *Lactobacillus delbrueckii subsp. bulgaricus* (ATCC 11842), a non-pathogenic surrogate strain with morphological and physical characteristics comparable to common SSI pathogens. The SWF was prepared by culturing the bacteria in a *Lactobacillus bulgaricus* agar medium (17154, Sigma-Aldrich, St. Louis, MO, USA). The experimental design included two SWF conditions representing different wound environments, to demonstrate the discriminative power of the RWCP: low pH (acidic) and high pH (buffered). For the low pH condition, the medium was prepared using agar at 7.6% (w/v) in distilled water, resulting in an initially acidic SWF pH of 5.8. For the high pH condition, 8% (v/v) acetate buffer (11.36% Sodium acetate, 0.99% Acetic acid; Sigma-Aldrich, St. Louis, MO, USA) was added to the medium, resulting in an initial slightly acidic SWF pH of

6.8. The total final volume of the SWF was 250 mL in both conditions. Given the relatively small buffer fraction, this dilution was not expected to substantially affect the bulk rheological properties of the SWF. Bacteria were cultured in the SWF at 37 °C for 48 h under gentle shaking. Then, the bacteria-containing SWF was subsequently maintained at 32-33 °C during experimental delivery. All preparation and delivery parameters (culture conditions, temperature, and syringe-pump flow rate) were identical across conditions, and three independent replicates were performed per condition, enabling a controlled comparison of pH-dependent effects.

2.3. Experimental protocol

Each experiment involved incision closure using a zipper-based wound-closure device (Senvok Medical, Lewes, DE, United States) followed by placement of a commercially available, widely used and market-leading wound dressing (ALLEVYN Gentle Border, 10 × 20 cm, Smith + Nephew, Hull, United Kingdom) over the incision wound

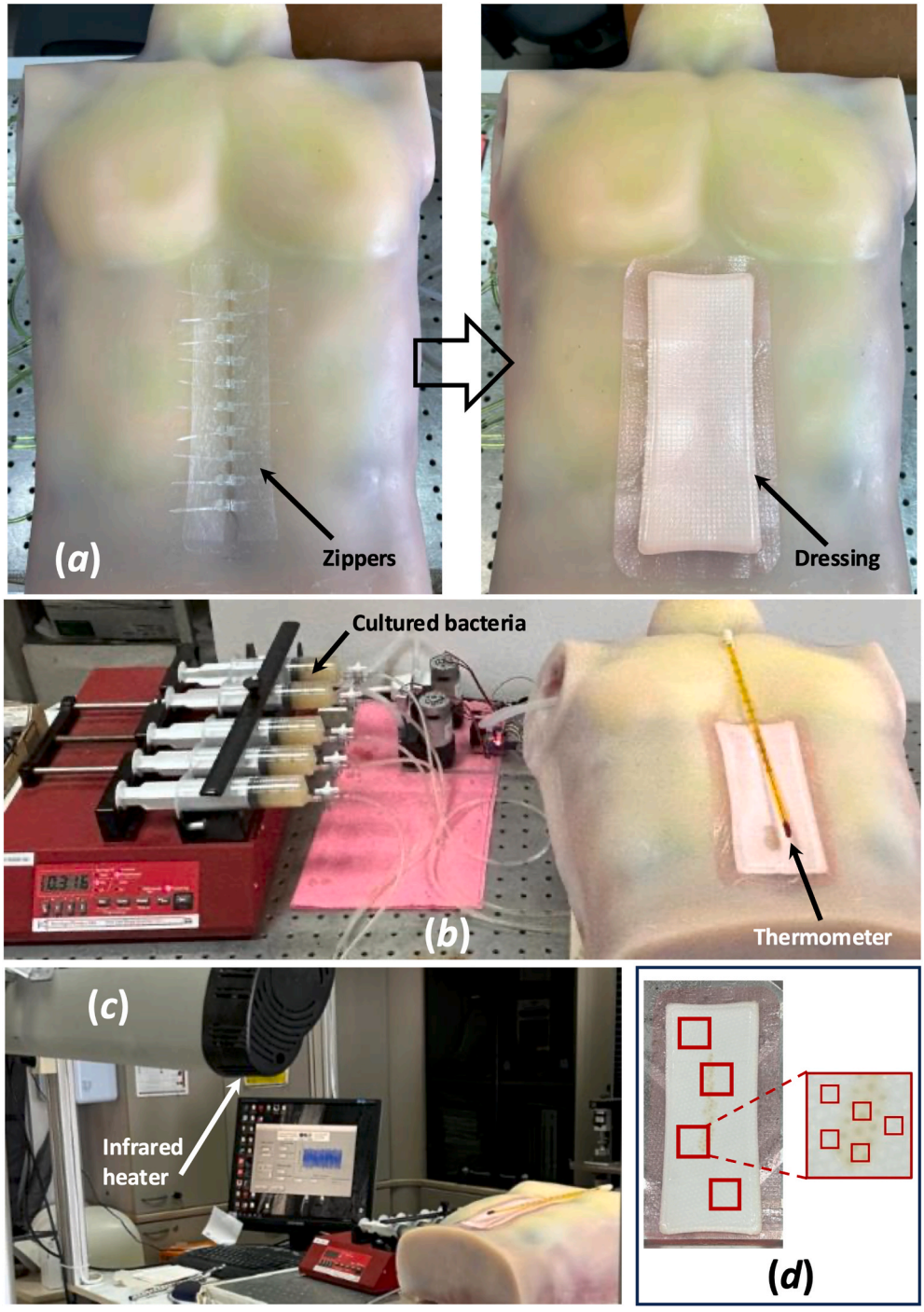

Fig. 3. The experimental setup for surgical site infection studies using a simulant wound fluid (SWF) containing live *Lactobacillus delbrueckii* subsp. bulgaricus: (a) Commercial zippers are used for primary closure, which is followed by application of a dressing to simulate clinical treatment of the incision wound. (b) The SWF with cultured live bacteria is delivered using a syringe pump. A thermometer for real-time temperature monitoring is included. (c) The temperature of the wound region is maintained at 32-33 °C using an external infrared heater, and is monitored throughout the experiment. (d) Multiple dressing samples are collected at experiment end-points for subsequent scanning electron microscopy studies including bacterial visualization and counting.

(Fig. 3a). Following SWF preloading and application of the dressing, the syringe pump was set to deliver the SWF at a rate of 0.23 mL/h, corresponding to a total delivered volume of 5.52 mL over 24 h (Fig. 3b). This flow rate is in agreement with our previously published robotic wound simulation studies using continuous low exudate flow conditions, and is clinically relevant as detailed in our published work [55]. The surface temperature of the wound and peri-wound region was monitored with a thermometer and maintained at 32-33 °C using an infrared heating lamp (Fig. 3b and c). After each experiment, the dressing was gently removed and allowed to dry for 24 h with the inner surface facing upward. Then, the dressing was cut into 1 × 3 cm samples for SEM imaging and further analysis, as follows.

2.4. Scanning electron microscopy and image processing

The dressing samples were coated with gold-palladium for 45 s, then mounted and examined under the SEM (Quanta 200F, FEI, Hillsboro, OR, USA) with settings of high vacuum, high voltage (5.0 kV), and magnification of ×7000. For each dressing (i.e., each independent experiment), at least 4 regions were imaged with at least 5 images per region (≥20 images per replicate). With three independent replicates per condition, this yielded ≥60 SEM images per pH condition (Fig. 3d). The SEM images were saved in TIFF format for further processing. Specifically, bacterial quantification on the used dressing samples was conducted using a combination of deep-learning segmentation and image analysis in FIJI (Fiji Is Just ImageJ, distribution version 2.16.0, URL: https://fiji.sc) which builds on ImageJ software for processing and analyzing scientific images (version 1.54p, URL: https://imagej.net/). Custom Python scripts were developed and used for software integration and bacterial parameter extraction. A custom-trained implementation of the Cellpose image segmentation algorithm [65], a deep learning-based tool, was adapted to recognize the specific morphology of *Lactobacillus delbrueckii subsp. bulgaricus* in the SEM images. First, a Cellpose deep learning model was trained on manually segmented SEM images to detect bacterial objects with high accuracy. The trained model was then applied in batch mode to segment all the remaining SEM images, generating pixel-wise segmentation masks and visual boundary annotations. False positive or false negative detections were corrected manually. The mask images were saved as PNG files and served as the basis for subsequent morphological and topological analyses. Representative examples of original SEM images versus Cellpose-processed images are shown in Fig. 4a and b (methodological details are provided in the **Appendix**).

2.5. Outcome measures and statistical analysis

To derive morphological parameters quantifying the bacterial contamination in the simulated incision wound, a custom macro script written in the ImageJ macro language was executed using FIJI. This macro performed high-throughput batch analysis on the Cellpose-generated mask images. Specifically, for each image, the script first applied a fixed intensity threshold, then converted the result to binary (Fig. 4c), and next used the "Analyze particles" function to extract the total number of bacterial objects, their area coverage as a percentage of the image, their circularity, roundness and aspect ratio. This process was performed automatically over entire image file directories, facilitating reproducibility and consistency across samples. In parallel, another custom Python script was developed to extract additional topological features from the same mask images, which was also designed for batch analyses. For each bacterium (area ≥10 pixels), the principal orientation

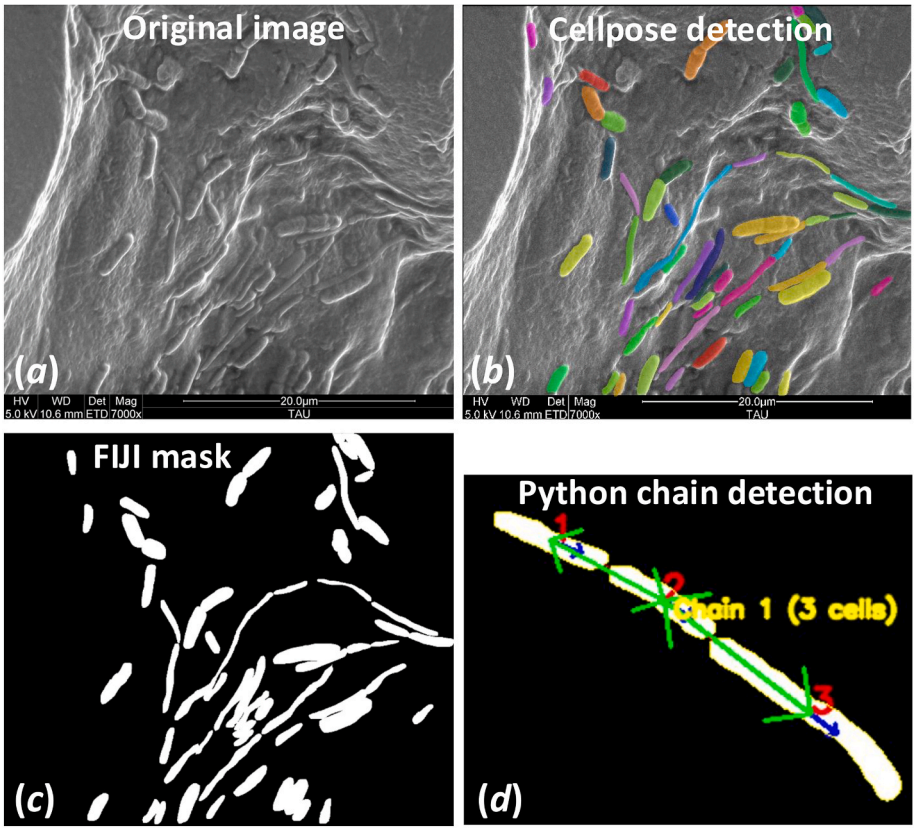

Fig. 4. Representative image processing pipeline of post-experimental dressing sample. (a) Original SEM image of *Lactobacillus delbrueckii* subsp. bulgaricus on dressing sample sputter-coated with gold-palladium, imaged at 5.0 kV under high vacuum conditions with a magnification of ×7000. (b) Cellpose deep learning segmentation of bacterial objects. (c) FIJI macro-generated binary mask used for morphological parameter extraction. (d) Representative output of the Python script showing a single detected bacterial chain (subset of a full image). The computational workflow and validation process are detailed in the **Appendix**.

of the microorganism was estimated via principal component analysis (PCA) with orientation normalized to 0-180°. Contours of the bacteria were extracted, and two 'tips' were defined for each identified bacterium as the extremal projections along the principal axis. Candidate neighboring bacteria were then screened with geometric and orientational criteria: components were linked when either: (i) the tip-to-tip distance was ≤20 pixels with inter-orientation difference ≤45°, and the inter-bacterial axis aligned with both principal axes (cos>0.4), or: (ii) the minimum contour-to-contour contact satisfied an edge-contact test enforcing axial alignment and limited lateral offset relative to the principal axis of each bacterium. A mutual best-match rule enforced only one matching neighbor per tip of a bacterium, preventing multiple bacteria linking through the same pole for the purpose of these analyses. The accepted links formed an undirected graph; 'chains' were then defined as connected components with no less than 3 contacting bacteria. For each image, the script outputted the number of chains, the mean and standard deviation (SD) of bacteria per chain, the total number of bacteria analyzed, and an annotated image showing the serial identification numbers of bacteria assigned by the code, the orientation of each bacterium in the image, and a chain coloring. Images were excluded from the final analyses, based on a Z-score retaining ≥ 95% of the images. A representative chain detection is shown in Fig. 4d (see the **Appendix** for algorithm details).

Image-level measurements were first averaged within each independent experiment (replicate), and statistical comparisons were performed on replicate-level means (n = 3 per condition). Descriptive statistics (mean ± SD) were calculated for number of bacteria, their percentage area coverage with respect to the image area, their circularity, roundness, aspect ratio, number of bacterial chains, and number of bacteria per chain. To identify potential statistically significant differences in the above outcome measures between the two pH conditions, independent two-sample, two-tailed Welch's *t*-tests were conducted for each metric, and a *p*-value lower than 0.05 was considered statistically significant. Data were organized and analyzed in Microsoft Excel (Microsoft Corporation, Redmond, WA, USA) and graphed using GraphPad Prism (version 8.4.2, GraphPad Software, San Diego, CA, USA).

These combined workflows facilitated automated, accurate and comprehensive quantification of bacterial colonization, their morphology, and spatial organization. The resulting metrics were then used for quantitative comparative analysis across the two experimental groups, i.e., low-versus high pH at the simulated wound site.

3. Results

We found ~45% significantly more bacteria on the dressing when the pH was low, however, the percentage of area covered by the bacteria did not differ significantly between the groups, indicating morphological changes which were confirmed through significant differences in the circularity, aspect ratio, and roundness outcome measures (Table 1 and Figs. 5 and 6). Specifically, under low, acidic pH conditions, the bacteria became less circular (circularity and roundness ↓; aspect ratio ↑), collectively indicating elongation of the bacterium in an acidic environment (Table 1 and Figs. 5 and 6). All values represent mean ± SD across three independent experiments per condition (n = 3). Further topological analysis of the chain structures formed by the bacteria revealed nearly fourfold more chains and 1.4-times larger chain assemblies under low pH conditions ($p \leq 0.02$), indicating that the acidic conditions support cooperative bacterial aggregation into structured chains. Notably, these chain formation trends aligned with the morphological elongation of the individual bacterium, suggesting that the unit elongation facilitates closer packing and stable associations between neighboring bacteria (Table 1 and Figs. 5 and 6).

Table 1
The outcome measures under high and low pH conditions. Values are presented as mean ± standard deviation across independent experiments (n = 3 per condition). Each experiment contributed ≥20 SEM images, which were averaged to obtain a single replicate-level value. ↑ = increase; ↓ = decrease; – = no trend.

Outcome measure	High, slightly acidic pH (6.8)	Low, acidic pH (5.8)	*p*-value	Trend of change for an acidic pH
Number of bacteria[a]	20.8 ± 0.5	30.1 ± 2.7	0.02	↑
Area coverage [%]	3.76 ± 0.17	3.63 ± 0.30	0.55	-
Circularity	0.57 ± 0.01	0.46 ± 0.02	0.004	↓
Aspect ratio	3.3 ± 0.2	4.5 ± 0.4	0.02	↑
Roundness	0.34 ± 0.01	0.25 ± 0.02	0.004	↓
# of chains	1.1 ± 0.7	4.2 ± 0.3	0.01	↑
# of bacteria in a chain	4.0 ± 0.5	5.6 ± 0.6	0.02	↑

[a] Counted in the field of view.

4. Discussion

This study reports, for the first time, a newly developed and validated RWCP system capable of simulating pathophysiologically and clinically relevant SSI conditions. By integrating the novel RWCP with a pathogen simulant and automated analyses of SEM micrographs, we established a standardized, reproducible platform that bridges preclinical assays and clinical wound care research. The RWCP reproduces key clinical features of infected laparotomy wounds, including exudate production, incision-treatment protocols, and importantly, potential bacterial colonization. In addition, the RWCP enabled detailed quantitative assessments of bacterial morphology and spatial organization under simulated wound conditions.

A key strength of this study is that, unlike previous robotic wound phantoms focusing on fluid handling or pressure simulations [52,54,55], this RWCP uniquely integrates biological infection simulation and bacterial growth analysis. This considerably expands the scope of wound-robotic research toward covering microbiological aspects, increasing its clinical relevance. Integration of microbiology and infection modeling into the RWCP was enabled by complementary, advanced computational tools. Specifically, deep learning-based segmentation of the bacteria using Cellpose software, FIJI morphometric analysis tool and custom Python algorithms enabled objective, automated high-throughput quantification of bacterial morphology and topology.

Our results showed that wound pH strongly influences bacterial colonization and organization (Table 1, Fig. 6), with low pH inducing elongated morphology and chain formation. These findings align with prior observations that low pH promotes elongation and chain formation in lactic acid bacteria [39,40], reinforcing the biological plausibility of the RWCP results. Together, these findings confirm that the RWCP sensitively detects microscale phenotypic and organizational adaptations, highlighting its potential as a discovery, validation and efficacy research platform for assessing environmental or therapeutic effects on surgical wound microbiology [66]. Our pipeline defines chains via geometry- and orientation-based neighbor linking on SEM images, enabling fully-automated morphology and topology quantification (Table 1, Fig. 6). While prior work described chaining of lactic acid bacteria and *Streptococci* only qualitatively [39,49,50], quantitative, automatically-acquired metrics of chain length and bacteria-per-chain had not yet been provided. To our knowledge, this is the first pipeline to provide fully-automated detection and quantification of bacterial chains in SEM images acquired from wound dressing specimens. The developed metrics, integrating structural and functional image analysis, offer a distinctive contribution to wound care related bioengineering and computational microbiology research.

The observed morphological and topological changes likely reflect adaptive strategies of the studied bacteria; it has been reported that

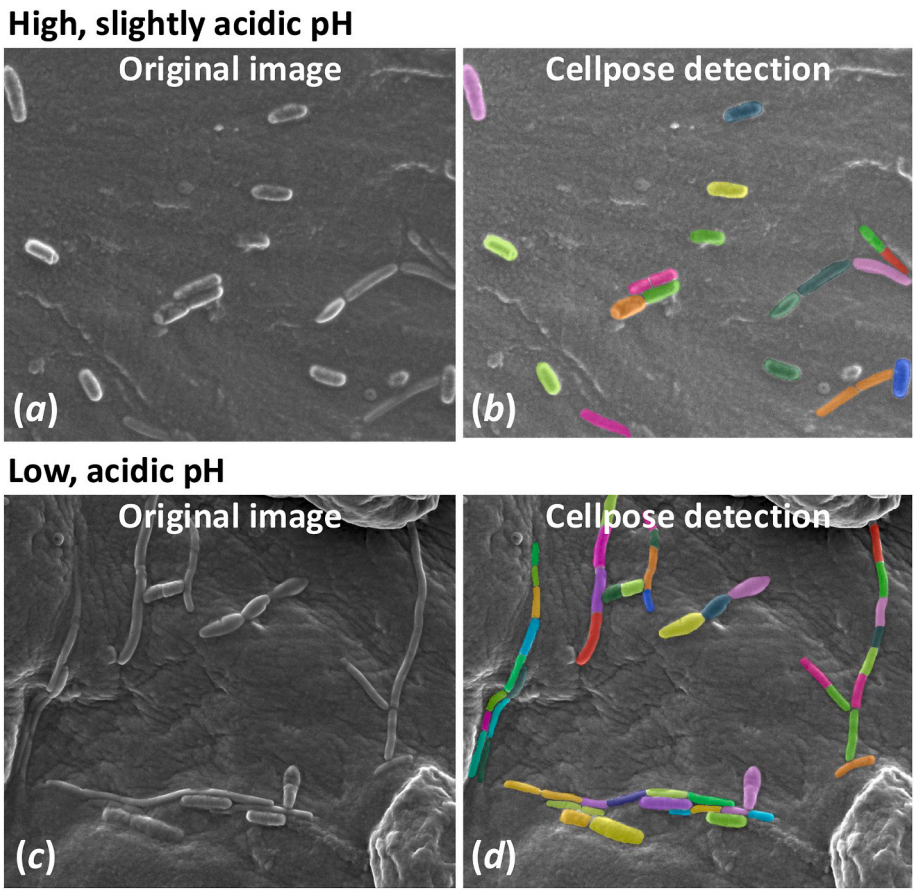

Fig. 5. Scanning electron microscopy (SEM) images of *Lactobacillus delbrueckii* subsp. bulgaricus on post-experimental dressing samples under different pH conditions. Dressings samples were sputter-coated with gold-palladium and imaged at 5.0 kV under high vacuum conditions with a magnification of ×7000: (a) Representative SEM image from the high pH group. (b) The same image after bacterial segmentation and quantification using the Cellpose software (deep learning–based image analysis tool). (c) Representative SEM image from the low pH group. (d) The same image after Cellpose-based analysis.

different bacteria minimize their exposed surface area under acidic or thermal stress (which is associated with membrane integrity and protein profile changes) for a more sustainable metabolism [36,39,40,67,68]. The RWCP nicely captured pH-dependent stress adaptations, highlighting its ability to detect not only static bacterial states but also potential resilience trajectories. The RWCP therefore has the potential to model complex multi-stressor environments relevant to wound complications, including surgical wounds that deteriorate to chronicity [69].

The RWCP addresses a critical gap in wound care research: The lack of standardized, reproducible, clinically relevant preclinical models for SSI research [22,23,28,70,71]. Traditional evaluations of wound dressings, including antibacterial types, often rely on heterogeneous RCTs which may be limited in power, patient population, clinical setting or scope, leading to uncertain effect estimates and low-quality evidence [20,21,72]. By providing controlled conditions and quantitative endpoints, the RWCP enables rigorous, statistically powered, and comparable preclinical benchmarks, supporting evidence-based clinical guidelines and addressing the lack of consistency in preclinical wound care studies [73]. Beyond laboratory validation, the RWCP can inform clinicians how antibacterial dressings perform in specific contaminated wound environments, offering a practical bridge to patient care. Importantly, our findings demonstrate that the RWCP detects subtle, environment-driven shifts in bacterial behavior, essential for evaluating not only antimicrobial efficacy but also broader impacts on wound microbiology and healing trajectories [70,74]. The clinically relevant RWCP may complement large RCTs, often challenging in wound care research, thereby facilitating technological progress and ultimately, contributing to improved SSI prevention strategies.

Despite the strengths of the RWCP, the current work has limitations. First, while *Lactobacillus delbrueckii subsp. bulgaricus* is a safe surrogate organism, it does not fully replicate the pathogenicity of clinically relevant SSI pathogens such as *Staphylococcus aureus* or *Escherichia coli*. Future work could incorporate clinically pathogenic strains, including antibiotic-resistant strains (e.g., MRSA), to enhance relevance for infection control and clinical translation [13,14]. Second, our study focused on short-term colonization (24 h), whereas SSIs typically evolve over days to weeks. Extending the experimental timeline, along with incorporating immune-mimicking components (e.g., neutrophil-like phantoms or cytokine gradients), could improve model fidelity. In addition, although the RWCP included controlled exudate flow into the simulated wound, the rheological properties of the SWF were not independently characterized. With that said, the SWF was not composed of pure water or saline, but of a nutrient-containing bacterial medium with dissolved solutes, so it functioned as a non-water carrier fluid rather than a purely aqueous solution [75,76]. Thus, although a minor effect of buffer addition on viscosity cannot be excluded, any such effect would be expected to be modest relative to the shared base medium composition. The SWF, which supported bacterial growth under standardized low-flow conditions, was hence considered a reasonable low-flow surrogate for exudate in this experimental context, while not representing the full rheological range of clinical wound exudate fluids [75–77]. Future work may therefore incorporate direct rheological measurements of the SWF to further refine its physiological realism and better approximate clinical wound environments. Beyond fluid properties, additional refinements may be needed to simulate other physiological and clinical parameters, such as immune interactions and

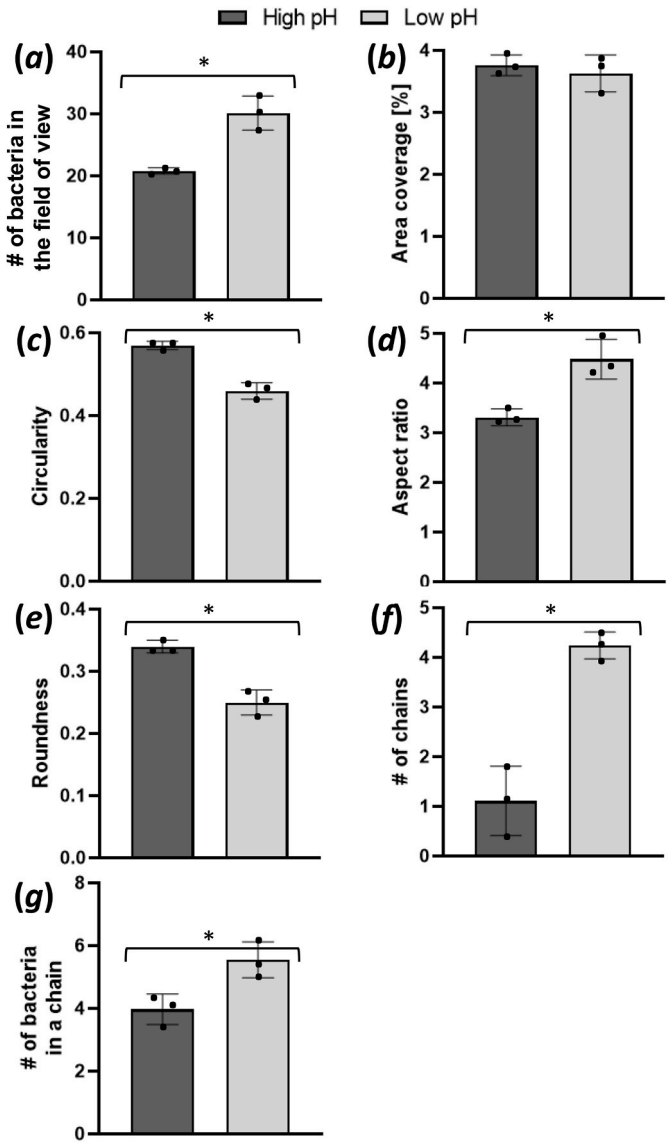

Fig. 6. Quantitative analysis of bacterial morphology and chain formation under high and low pH conditions. Bars show mean ± standard deviation across independent experiments (n = 3 per condition); each data point represents the mean of ≥20 SEM images from a single dressing/experiment. (a) Number of bacteria per image. (b) Bacterial area coverage [%]. (c) Circularity. (d) Aspect ratio. (e) Roundness. (f) Number of bacterial chains. (g) Average number of bacteria per chain. Low pH conditions were associated with significantly higher bacterial counts, increased aspect ratio, and more extensive chain formation and bacteria per chain, whereas circularity and roundness were reduced. Area coverage did not differ significantly between groups. Statistical significance was determined using Welch's *t*-test, with $p < 0.05$ considered significant.

prophylactic antibiotic treatments. Moreover, the computational pipeline, while robust, will require adaptation for a wider range of bacterial species and substrate types to become broadly applicable. Future applications may assess diverse wound-care technologies under realistic conditions, including silver-ion, honey, iodine dressings, single-use NPWT systems, and varied dressing protocols [78]. The RWCP may also be expanded to simulate high-risk conditions such as diabetic or ischemic wounds, which carry elevated SSI risk and often respond poorly to conventional therapies [23].

To conclude, the new RWCP system represents a significant methodological advancement in wound care research, providing a reproducible, ethically sustainable, and clinically relevant robust platform for studying SSIs. The demonstrated sensitivity of the RWCP underscores its potential as a benchmark laboratory system for both experimental validation and translational evaluation of wound care products and treatments. Collectively, this work sets the foundation for integrating biomechanical, microbiological, and computational data into unified preclinical testing standards for SSI mitigation. In the longer term, the RWCP could support industry efficacy research, as well as development of tailored treatment algorithms where clinical decisions are informed by quantitative, preclinically validated data on how specific wound environments affect both the bacterial dynamics and dressing performance. Together, these advances position the RWCP as a standardized preclinical system for testing SSI-relevant wound care technologies and products, streamlining such evaluations and informing evidence-based practice.

Declaration of competing interest

The authors declare that they have no conflict of interest.

Acknowledgements

This work was partially supported by the Israeli Ministry of Innovation, Science and Technology: Breakthrough Research Program Grant no. 1001702603, awarded to Professor Amit Gefen in 2023. The authors thank the team of the Environmental Scanning Electron Microscopy (SEM) Laboratory at the Wolfson Applied Materials Research Centre of Tel Aviv University for their technical assistance with the SEM image acquisition.

APPENDIX

Deep-learning segmentation and topology analysis: Training and validation

From the available dataset, 80 SEM images representing both experimental conditions (i.e., high and low pH) were randomly selected for model development and evaluation. An initial training set of 50 images (corresponding to approximately 1000 to 1500 bacterial instances, Table 1) was used for preliminary segmentation using the pretrained cyto3 model implemented in Cellpose. Predicted masks generated by this model were manually reviewed and amended, if necessary, within the Cellpose interface, to correct false negative and false positive detections, thereby generating ground-truth segmentation masks for supervised training. The final masks were exported as PNG-format images.

Model training was performed using single-channel input (NChan = 1), object diameter = 30 pixels, flow threshold = 0.07, the RAdam optimizer (learning rate = 0.001), and 300 training epochs. The dataset was partitioned into independent training (n = 50), validation (n = 15), and test (n = 15) subsets with no overlap between the sets. No images from the validation or test subsets were used for the training or hyperparameter tuning. Training and validation losses were monitored throughout the training process to confirm stable convergence and absence of overfitting.

Segmentation performance was evaluated on the independent test set at the object level using the Cellpose evaluation metrics, which define true positive detections based on an intersection-over-union (IoU) threshold of 0.5. The test set comprised 15 SEM images, corresponding to approximately 300-450 individual bacterial instances evaluated at the object level. For previously unseen images, the model achieved precision of 87.1%, recall of 85.7%, and F1-score of 86.4%. Performance metrics were computed at the object level to reflect the detection accuracy across individual bacterial instances rather than an image-level agreement. A representative comparison between manual annotation and model prediction from the test set is shown in Figure A.1.

For the full experimental dataset, automated segmentation outputs were subsequently subjected to minor manual quality control and corrections, to fix occasional mis-segmentations prior to downstream quantitative analysis. In parallel, a custom Python script was developed to extract additional topological features from the same mask images and implemented for batch analysis. For each bacterium (area $\geq$10 pixels), principal orientation was estimated using principal component analysis (PCA), with orientation normalized to 0-180°. Two terminal "tip" points were defined along the major axis of each bacterium based on extremal projections.

Candidate neighboring bacteria were screened using geometric and orientational criteria. Two bacteria were considered connected if either: (i) the tip-to-tip distance was $\leq$20 pixels with an inter-orientation difference $\leq$45°, and the inter-bacterial axis aligned with both principal axes (cosine similarity >0.4), or (ii) the minimum contour-to-contour contact satisfied an edge-alignment test enforcing axial proximity and limited lateral offset relative to the principal axis. A mutual best-match rule allowed only one neighboring bacterium per tip, preventing multiple links through the same pole.

Threshold parameters (20 pixels for tip-to-tip distance and 45° for inter-orientation difference) were determined through structured empirical tuning within a biologically plausible parameter space. Candidate parameter values were systematically varied while executing the full detection pipeline to ensure stable, biologically consistent chain identification and minimize spurious neighbor linkages. Sensitivity analyses confirmed that moderate variations around the selected values (18-22 pixels and 42-48°, respectively) did not substantially affect chain counts or bacteria-per-chain metrics, supporting robustness of the topology criteria.

Chains were defined as connected sequences of three or more bacteria, formed through consecutive neighbor linkages. For each image, the script quantified the number of chains and the mean number of bacteria per chain for subsequent statistical comparison between pH conditions. To further verify analytical rigor, a representative subset of SEM images (n = 20; balanced across high and low pH conditions) was independently inspected to define bacterial chains and number of bacteria per chain according to the same $\geq$3-bacteria criterion. Automated chain assignments were compared with manual visual classification at the chain level, demonstrating high concordance in both chain detection and chain length estimation. A representative example of manual classification and algorithm visualization is provided in Figure A.2.

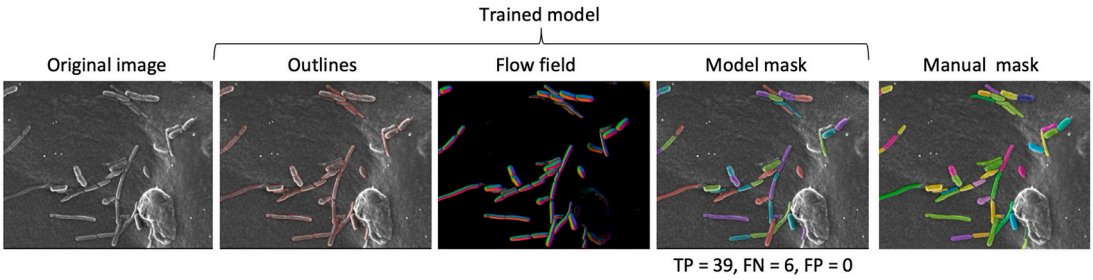

Fig. A.1. Representative example of manual ground-truth annotation and automated segmentation using the trained Cellpose model. From left to right: original SEM image, predicted outlines, predicted flow field, model-generated instance mask, and manual ground-truth mask. In this example, 45 bacteria were manually annotated and 39 were correctly detected (True positive = 39, False negative = 6, False positive = 0).

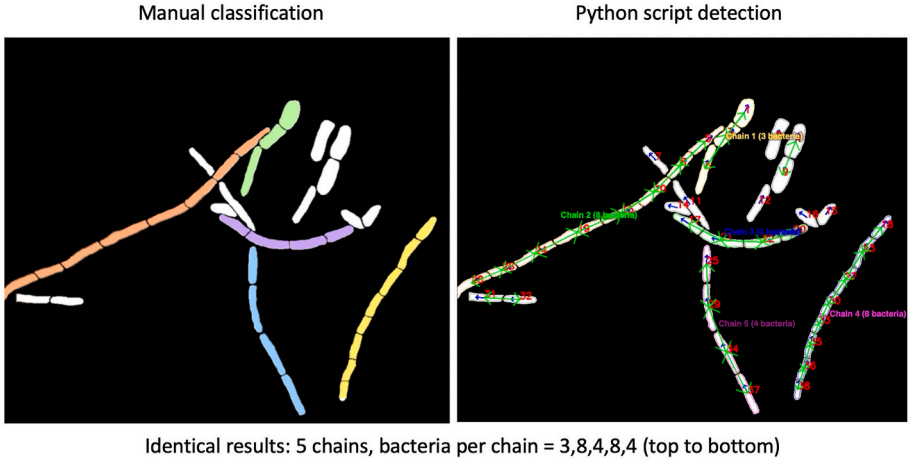

Fig. A.2. Representative example of topology-based bacterial chain identification. Left frame: Automated chain assignment with each detected chain colored separately (chains were defined as connected components containing $\geq$3 bacteria). Right frame: Full algorithm visualization including principal orientation vectors and geometric linkage criteria. The automated detection is consistent with a manual visual classification.

References

[1] Agency for Healthcare Research and Quality. Rockville, MD. Agency for healthcare research and quality [cited 2025 Jun 19]. Surgical Site Infections. Available from: https://psnet.ahrq.gov/primer/surgical-site-infections; 2024.

[2] Sahebally SM, McKevitt K, Stephens I, Fitzpatrick F, Deasy J, Burke JP, et al. Negative pressure wound therapy for closed laparotomy incisions in general and colorectal surgery: a systematic review and meta-analysis. JAMA Surg 2018 Nov 1; 153(11):e183467. https://doi.org/10.1001/jamasurg.2018.3467.

[3] WHO. Global guidelines for the prevention of surgical site infection [Internet]. second ed. Geneva: World Health Organization; 2018 [cited 2025 Jun 19]. Available from: https://www.who.int/publications/i/item/9789241550475.

[4] Avsar P, Patton D, Sayeh A, Ousey K, Blackburn J, O'Connor T, et al. The impact of care bundles on the incidence of surgical site infections: a systematic review. Adv Skin Wound Care 2022 Jul 1;35(7):386–93. https://doi.org/10.1097/01.ASW.0000831080.51977.0b.

[5] Chadwick P, Ousey K. Bacterial-binding dressings in the management of wound healing and infection prevention: a narrative review. J Wound Care 2019 Jun 2;28 (6):370–82. https://doi.org/10.12968/jowc.2019.28.6.370.

[6] Centers for Disease Control and Prevention. Surgical site infection event (SSI). 2025. Atlanta, GA.

[7] Berríos-Torres SI, Umscheid CA, Bratzler DW, Leas B, Stone EC, Kelz RR, et al. Centers for disease control and prevention guideline for the prevention of surgical site infection, 2017. JAMA Surg 2017 Aug 1;152(8):784–91. https://doi.org/10.1001/jamasurg.2017.0904.

[8] Lima JL, de Aguiar RA, Leite HV, Silva HH, de Oliveira WM, Sacramento JP, Wakabayashi EA, de Souza HC, Clemente WT, Romanelli RM. Surveillance of surgical site infection after cesarean section and time of notification. Am J Infect Control 2016 Mar 1;44(3):273–7. https://doi.org/10.1016/j.ajic.2015.10.022.

[9] Elangovan S, Murali S, Aravindhan A, Seow CS, Graves N. Systematic review and meta-analysis of outcomes associated with incisional and organ/space surgical site infections in abdominal surgery patients. Antimicrobial resistance and infection control. BioMed Central Ltd; 2025. https://doi.org/10.1186/s13756-025-01656-w.

[10] Calderwood MS, Kleinman K, Huang SS, Murphy MV, Yokoe DS, Platt R. Surgical site infections: volume-outcome relationship and year-to-year stability of performance rankings. Med Care 2017 Jan;55(1):79–85. https://doi.org/10.1097/MLR.0000000000000620.

[11] Napolitano F, Tomassoni D, Cascone D, Di Giuseppe G, Group TCW. Evaluation of hospital readmissions for surgical site infections in Italy. Eur J Publ Health 2018 Jun 1;28(3):421–5. https://doi.org/10.1093/eurpub/ckx205.

[12] Kirby JP, Mazuski JE. Prevention of surgical site infection. Surg Clin 2009;89(2): 365–89. https://doi.org/10.1016/j.suc.2009.01.001.

[13] Engemann JJ, Carmeli Y, Cosgrove SE, Fowler VG, Bronstein MZ, Trivette SL, et al. Adverse clinical and economic outcomes attributable to methicillin resistance among patients with Staphylococcus aureus surgical site infection. Clin Infect Dis 2003 Mar 1;36(5):592–8. https://doi.org/10.1086/367653.

[14] Manian FA, Meyer PL, Setzer J, Senkel D. Surgical site infections associated with methicillin-resistant staphylococcus aureus: do postoperative factors play a role? Clin Infect Dis 2003 Apr 1;36(7):863–8. https://doi.org/10.1086/368195.

[15] Ban KA, Minei JP, Laronga C, Harbrecht BG, Jensen EH, Fry DE, et al. American college of surgeons and surgical infection society: surgical site infection guidelines, 2016 update. J Am Coll Surg 2017 Jan 1;224(1):59–74. https://doi.org/10.1016/j.jamcollsurg.2016.10.029.

[16] Ayello EA. How to culture a wound. Nursing (Brux) 2002;32(12):10. https://doi.org/10.1097/00152193-200212000-00003.

[17] Norman G, Goh EL, Dumville JC, Shi C, Liu Z, Chiverton L, et al. Negative pressure wound therapy for surgical wounds healing by primary closure. Cochrane Database Syst Rev 2020 May 1;5. https://doi.org/10.1002/14651858.CD009261.pub5.

[18] Horgan S, Hegarty J, Drennan J, Keane D, Saab MM. The effect of interventions on the incidence of surgical site infections in acute care settings: a systematic review. J Tissue Viability Tissue Viability Society 2024:75–88. https://doi.org/10.1016/j.jtv.2023.11.004.

[19] Darwin E, Tomic-Canic M. Healing chronic wounds: current challenges and potential solutions. Curr Dermatol Rep Curr Med Group LLC 2018;1:296–302. https://doi.org/10.1007/s13671-018-0239-4.

[20] Gottrup F, Apelqvist J. The challenge of using randomized trials in wound healing. Br J Surg 2010;97(3):303–4. https://doi.org/10.1002/bjs.7030.

[21] NICE. Chronic wounds: advanced wound dressings and antimicrobial dressings evidence summary key points from the evidence. 2016. Report.

[22] Grada A, Mervis J, Falanga V. Research techniques made simple: animal models of wound healing. J Invest Dermatol 2018:2095–105. https://doi.org/10.1016/j.jid.2018.08.005. Elsevier B.V.

[23] Nunan R, Harding KG, Martin P. Clinical challenges of chronic wounds: searching for an optimal animal model to recapitulate their complexity. Dis Model Mech 2014 Nov 1;7(11):1205–13. https://doi.org/10.1242/dmm.016782.

[24] Alves DR, Booth SP, Scavone P, Schellenberger P, Salvage J, Dedi C, et al. Development of a high-throughput ex-vivo burn wound model using porcine skin, and its application to evaluate new approaches to control wound infection. Front Cell Infect Microbiol 2018 Jun;15:8. https://doi.org/10.3389/fcimb.2018.00196.

[25] Yang Q, Phillips PL, Sampson EM, Progulske-Fox A, Jin S, Antonelli P, et al. Development of a novel ex vivo porcine skin explant model for the assessment of mature bacterial biofilms. Wound Repair Regen 2013 Sep;21(5):704–14. https://doi.org/10.1111/wrr.12074.

[26] Coenye T, Nelis HJ. In vitro and in vivo model systems to study microbial biofilm formation. J Microbiol Methods 2010:89–105. https://doi.org/10.1016/j.mimet.2010.08.018.

[27] Lorenz K, Preem L, Sagor K, Putrinš M, Tenson T, Kogermann K. Development of in vitro and Ex vivo biofilm models for the assessment of antibacterial fibrous electrospun wound dressings. Mol Pharm 2023 Feb 6;20(2):1230–46. https://doi.org/10.1021/acs.molpharmaceut.2c00902.

[28] Saeed S, Martins-Green M. Assessing animal models to study impaired and chronic wounds. Int J mol sci. Multidisciplinary Digital Publishing Institute (MDPI); 2024. p. 3837. https://doi.org/10.3390/ijms25073837.

[29] Percival SL, McCarty S, Hunt JA, Woods EJ. The effects of pH on wound healing, biofilms, and antimicrobial efficacy. Wound Repair Regen: Offic Publ Wound Healing Soc European Tissue Repair Soc 2014:174–86. https://doi.org/10.1111/wrr.12125.

[30] Schneider LA, Korber A, Grabbe S, Dissemond J. Influence of pH on wound-healing: a new perspective for wound-therapy? Arch Dermatol Res 2007:413–20. https://doi.org/10.1007/s00403-006-0713-x.

[31] Chekli Y, Thiriet-Rupert S, Caillet C, Quilès F, Le Cordier H, Deshayes E, et al. Biophysical insights into sugar-dependent medium acidification promoting YfaL protein-mediated Escherichia coli self-aggregation, biofilm formation and acid stress resistance. Nanoscale 2024 Aug 17;16(37):17567–84. https://doi.org/10.1039/d4nr01884b.

[32] Isom LL, Khambatta ZS, Moluf JL, Akers DF, Martin SE. Filament formation in Listeria monocytogenes. J Food Protect 1995 Sep;58(9):1031–3. https://doi.org/10.4315/0362-028X-58.9.1031.

[33] Khan F, Jeong GJ, Tabassum N, Mishra A, Kim YM. Filamentous morphology of bacterial pathogens: regulatory factors and control strategies. Applied microbiology and biotechnology. Springer Science and Business Media Deutschland GmbH; 2022. p. 5835–62. https://doi.org/10.1007/s00253-022-12128-1.

[34] Liu Y, Zhang J, Ji Y. Environmental factors modulate biofilm formation by Staphylococcus aureus. Science progress. SAGE Publications Ltd; 2020. https://doi.org/10.1177/0036850419898659.

[35] Papadimitriou K, Alegría Á, Bron PA, de Angelis M, Gobbetti M, Kleerebezem M, et al. Stress physiology of lactic acid bacteria. Microbiol Mol Biol Rev 2016 Sep;80 (3):837–90. https://doi.org/10.1128/mmbr.00076-15.

[36] Streit F, Delettre J, Corrieu G, Béal C. Acid adaptation of Lactobacillus delbrueckii subsp. bulgaricus induces physiological responses at membrane and cytosolic levels that improves cryotolerance. J Appl Microbiol 2008;105(4):1071–80. https://doi.org/10.1111/j.1365-2672.2008.03848.x. PubMed PMID: 18498349.

[37] Vinderola CG, Reinheimer JA. Lactic acid starter and probiotic bacteria: a comparative "in vitro" study of probiotic characteristics and biological barrier resistance. Food Res Int 2003;36(9–10):895–904. https://doi.org/10.1016/S0963-9969(03)00098-X.

[38] Zhai Z, Douillard FP, An H, Wang G, Guo X, Luo Y, et al. Proteomic characterization of the acid tolerance response in Lactobacillus delbrueckii subsp. bulgaricus CAUH1 and functional identification of a novel acid stress-related transcriptional regulator Ldb0677. Environ Microbiol 2014 Jun 1;16(6):1524–37. https://doi.org/10.1111/1462-2920.12280.

[39] Ingham CJ, Beerthuyzen M, Vlieg JVH. Population heterogeneity of Lactobacillus plantarum WCFS1 microcolonies in response to and recovery from acid stress. Appl Environ Microbiol 2008 Dec;74(24):7750–8. https://doi.org/10.1128/AEM.00982-08.

[40] Venugopal A, Steinberg D, Moyal O, Yonassi S, Glaicher N, Gitelman E, et al. Computational analysis of morphological changes in Lactiplantibacillus plantarum under acidic stress. Microorganisms 2025 Mar 12;13(3):647. https://doi.org/10.3390/microorganisms13030647.

[41] Chen S, Niu H, Wu Y, Sun J, Han X, Zhang L. Influence of lactic acid on cell cycle progressions in Lactobacillus bulgaricus during batch culture. Appl Biochem Biotechnol 2021 Mar 1;193(3):912–24. https://doi.org/10.1007/s12010-020-03459-8.

[42] Divakar T, Srivastava R. Surface pH and acute burn wound healing. Indian J Burns 2019;27(1):57. https://doi.org/10.4103/ijb.ijb_19_19.

[43] Sharpe JR, Booth S, Jubin K, Jordan NR, Lawrence-Watt DJ, Dheansa BS. Progression of wound pH during the course of healing in burns. J Burn Care Res 2013 May;34(3):201–8. https://doi.org/10.1097/BCR.0b013e31825d5569.

[44] Jeckel H, Drescher K. Advances and opportunities in image analysis of bacterial cells and communities. FEMS Microbiol Rev 2021 Jul 1;45(4). https://doi.org/10.1093/femsre/fuaa062.

[45] Hartmann R, Jeckel H, Jelli E, Singh PK, Vaidya S, Bayer M, et al. Quantitative image analysis of microbial communities with BiofilmQ. Nat Microbiol 2021: 151–6. https://doi.org/10.1038/s41564-020-00817-4.

[46] Ragi S, Rahman MH, Duckworth J, Jawaharraj K, Chundi P, Gadhamshetty V. Artificial intelligence-driven image analysis of bacterial cells and biofilms. IEEE ACM Trans Comput Biol Bioinf 2023 Jan 1;20(1):174–84. https://doi.org/10.1109/TCBB.2021.3138304.

[47] Rahman MH, Azam MA, Hossen MA, Ragi S, Gadhamshetty V. BiofilmScanner: a computational intelligence approach to obtain bacterial cell morphological attributes from biofilm image. IEEE ACM Trans Comput Biol Bioinf 2023 Jul 24: 1–11. https://doi.org/10.48550/arXiv.2302.09629.

[48] Syvertsson S, Vischer NOE, Gao Y, Hamoen LW. When phase contrast fails: chaintracer and NucTracer, two ImageJ methods for semi-automated single cell analysis using membrane or DNA staining. PLoS One 2016 Mar 1;11(3). https://doi.org/10.1371/journal.pone.0151267.

[49] Domenech A, Slager J, Veening JW. Antibiotic-induced cell chaining triggers pneumococcal competence by reshaping quorum sensing to autocrine-like signaling. Cell Rep 2018 Nov 27;25(9):2390–400. https://doi.org/10.1016/j.celrep.2018.11.007.

[50] Rodriguez JL, Dalia AB, Weiser JN. Increased chain length promotes pneumococcal adherence and colonization. Infect Immun 2012 Oct;80(10):3454–9. https://doi.org/10.1128/IAI.00587-12.
[51] Sroka-Oleksiak A, Pardyl A, Rymarczyk D, Olechowska-Jarząb A, Biegun-Drożdż K, Ochońska D, et al. AI-Driven rapid identification of bacterial and fungal pathogens in blood smears of septic patients. Comput Biol Med 2025 Nov;22:199–111328. https://doi.org/10.1016/j.compbiomed.2025.111328.
[52] Lustig A, Gefen A. Three-dimensional shape-conformation performances of wound dressings tested in a robotic sacral pressure ulcer phantom. Int Wound J 2021 Oct 1;18(5):670–80. https://doi.org/10.1111/iwj.13569.
[53] Lustig A, Gefen A. Fluid management and strength postsimulated use of primary and secondary dressings for treating diabetic foot ulcers: robotic phantom studies. Int Wound J 2022 Feb 1;19(2):305–15. https://doi.org/10.1111/iwj.13631.
[54] Orlov A, Gefen A. Fluid handling performance of wound dressings tested in a robotic venous leg ulcer system under compression therapy. Int Wound J 2023 May 1;20(5):1384–92. https://doi.org/10.1111/iwj.13985. PubMed PMID: 36267049.
[55] Orlov A, Ciliberti M, Somma R, Gefen A. A robotic venous leg ulcer system reveals the benefits of negative pressure wound therapy in effective fluid handling. Int Wound J 2024 Feb 1;21(2):e14426. https://doi.org/10.1111/iwj.14426.
[56] Orlov A, Lustig A, Grigatti A, Gefen A. Fluid handling dynamics and durability of silver-containing gelling fiber dressings tested in a robotic wound system. Adv Skin Wound Care 2022 Jun 1;35(6):326–34. https://doi.org/10.1097/01.ASW.0000823972.16446.ff.
[57] Xu F, Lu TJ. Chapter 3 skin biothermomechanics: modeling and experimental characterization. Adv Appl Mech 2009;Adv Appl Mechanics43:147–248. doi: 10.1016/S0065-2156(09)43003-5.
[58] Mostafavi Yazdi SJ, Baqersad J. Mechanical modeling and characterization of human skin: a review. J Biomech 2022. https://doi.org/10.1016/j.jbiomech.2021.110864. Elsevier Ltd.
[59] Kuthe CD, Uddanwadiker RV. Investigation of effect of fiber orientation on mechanical behavior of skeletal muscle. J Appl Biomater Funct Mater 2016;14(2):e154–62. https://doi.org/10.5301/jabfm.5000275.
[60] Morrow DA, Haut Donahue TL, Odegard GM, Kaufman KR. Transversely isotropic tensile material properties of skeletal muscle tissue. J Mech Behav Biomed Mater 2010 Jan;3(1):124–9. https://doi.org/10.1016/j.jmbbm.2009.03.004.
[61] Koruk H, Rajagopal S, de Melo Baesso R, Alvarenga AV, Kontomaris SV. A review on the identification of the mechanical properties of soft tissues and tissue-mimicking phantoms. J Mech Behav Biomed Mater 2026 May;177:107371. https://doi.org/10.1016/j.jmbbm.2026.107371.
[62] Palevski A, Glaich I, Portnoy S, Linder-Ganz E, Gefen A. Stress relaxation of porcine gluteus muscle subjected to sudden transverse deformation as related to pressure sore modeling. J Biomech Eng 2006 Oct;128(5):782–7. https://doi.org/10.1115/1.2264395.
[63] Aleksei Orlov, Gefen A. Skin mechanobiology: from basic science to clinical applications. In: Luc Téot, Meaume S, editors. Skin necrosis. Cham: Springer Nature Switzerland; 2024. p. 73–80. https://doi.org/10.1007/978-3-031-60954-1_9. AS and DMV and PS.
[64] Gefen A, Haberman E. Viscoelastic properties of ovine adipose tissue covering the gluteus muscles. J Biomech Eng 2007 Dec;129(6):924–30. https://doi.org/10.1115/1.2800830.
[65] Stringer C, Wang T, Michaelos M, Pachitariu M. Cellpose: a generalist algorithm for cellular segmentation. Nat Methods 2021 Jan 1;18(1):100–6. https://doi.org/10.1038/s41592-020-01018-x.
[66] Weigelt MA, Lev-Tov HA, Tomic-Canic M, Lee WD, Williams R, Strasfeld D, et al. Advanced wound diagnostics: toward transforming wound care into precision medicine. Adv Wound Care 2022 Jun 1;11(6):330–59. https://doi.org/10.1089/wound.2020.1319.
[67] Cayron J, Dedieu-Berne A, Lesterlin C. Bacterial filaments recover by successive and accelerated asymmetric divisions that allow rapid post-stress cell proliferation. Mol Microbiol 2023 Feb 1;119(2):237–51. https://doi.org/10.1111/mmi.15016.
[68] Zhang X, Zheng Y, Zhou C, Cao J, Pan D, Cai Z, et al. Comparative physiological and transcriptomic analysis of sono-biochemical control over post-acidification of Lactobacillus delbrueckii subsp. Bulgaricus Food Microbiol 2024 Sep 1;122:104563. https://doi.org/10.1016/j.fm.2024.104563.
[69] Pastar I, Stojadinovic O, Yin NC, Ramirez H, Nusbaum AG, Sawaya A, et al. Epithelialization in wound healing: a comprehensive review. Adv Wound Care 2014 Jul;3(7):445–64. https://doi.org/10.1089/wound.2013.0473.
[70] Malone M, Schultz G. Challenges in the diagnosis and management of wound infection. Br J dermatol. John Wiley and Sons Inc; 2022. p. 159–66. https://doi.org/10.1111/bjd.21612.
[71] Eming SA, Martin P, Tomic-Canic M. Wound repair and regeneration: mechanisms, signaling, and translation. Sci Transl Med 2014:265sr5. https://doi.org/10.1126/scitranslmed.3009337. American Association for the Advancement of Science.
[72] Gottrup F, Apelqvist J, Price P. Outcomes in controlled and comparative studies on non-healing wounds recommendations to improve the quality of evidence in wound management. J Wound Care 2010 Jan;19(6):237–68. https://doi.org/10.12968/jowc.2010.19.6.48471.
[73] Ojeh N, Vecin NM, Pastar I, Volk SW, Wilgus T, Griffiths S, et al. The wound reporting in animal and human preclinical studies guidelines. Wound Repair Regen 2025 Jan 1;33(1). https://doi.org/10.1111/wrr.13232.
[74] Beraja GE, Gruzmark F, Pastar I, Lev-Tov H. What's new in wound healing: treatment advances and microbial insights. Am J Clin Dermatol 2025 Sep 1;26(5):677–94. https://doi.org/10.1007/s40257-025-00953-9.
[75] Gefen A, Alves P, Beeckman D, Cullen B, Lázaro-Martínez JL, Lev-Tov H, et al. Fluid handling by foam wound dressings: from engineering theory to advanced laboratory performance evaluations. Int Wound J 2024 Feb 1;21(2). https://doi.org/10.1111/iwj.14674.
[76] Svensby AU, Nygren E, Gefen A, Cullen B, Ronkvist ÅM, Gergely AB, et al. The importance of the simulated wound fluid composition and properties in the determination of the fluid handling performance of wound dressings. Int Wound J 2024 May 1;21(5). https://doi.org/10.1111/iwj.14861.
[77] Lustig A, Alves P, Call E, Santamaria N, Gefen A. The sorptivity and durability of gelling fibre dressings tested in a simulated sacral pressure ulcer system. Int Wound J 2021 Apr 1;18(2):194–208. https://doi.org/10.1111/iwj.13515.
[78] Chen V, Burgess JL, Verpile R, Tomic-Canic M, Pastar I. Novel diagnostic technologies and therapeutic approaches targeting chronic wound biofilms and microbiota. Curr Dermatol Rep 2022:60–72. https://doi.org/10.1007/s13671-022-00354-9. Springer.